



Deterministic inverse design of Tamm plasmon thermal emitters with multi-resonant control

Mingze He^{1,6} , J. Ryan Nolen^{2,6}, Josh Nordlander³, Angela Cleri³, Nathaniel S. Mcllwaine³, Yucheng Tang⁴, Guanyu Lu¹ , Thomas G. Folland^{1,5}, Bennett A. Landman⁴, Jon-Paul Maria³ and Joshua D. Caldwell^{1,4} 

Wavelength-selective thermal emitters (WS-EMs) are of interest due to the lack of cost-effective, narrow-band sources in the mid- to long-wave infrared. WS-EMs can be realized via Tamm plasmon polaritons (TPPs) supported by distributed Bragg reflectors on metals. However, the design of multiple resonances is challenging as numerous structural parameters must be optimized simultaneously. Here we use stochastic gradient descent to optimize TPP emitters (TPP-EMs) composed of an aperiodic distributed Bragg reflector deposited on doped cadmium oxide (CdO) film, where layer thicknesses and carrier density are inversely designed. The combination of the aperiodic distributed Bragg reflector with the designable plasma frequency of CdO enables multiple TPP-EM modes to be simultaneously designed with arbitrary spectral control not accessible with metal-based TPPs. Using this approach, we experimentally demonstrated and numerically proposed TPP-EMs exhibiting single or multiple emission bands with designable frequencies, line-widths and amplitudes. This thereby enables lithography-free, wafer-scale WS-EMs that are complementary metal-oxide-semiconductor compatible for applications such as free-space communications and gas sensing.

The development of cheap and effective light sources in the infrared is highly desired for numerous applications. These range from free-space communications and infrared beacons to bar-codes and could improve our ability to monitor environmental pollutants and toxins through molecular sensing metrologies, such as non-dispersive infrared (NDIR) sensing^{1–3}. Thus, WS-EMs are of particular interest due to the lack of cost-effective light sources in the mid- to long-wave infrared (MWIR, LWIR)⁴. Most proposed WS-EMs employ patterned nanostructures^{1,4–11}, thereby requiring high-cost, low-throughput lithographic methods, and are therefore inappropriate for many applications. An alternative solution is TPP heterostructures¹². Such TPP structures consist of a distributed Bragg reflector (DBR) on a conductor (Fig. 1a), typically a noble metal, where the DBR provides optical phase matching to the metal surface, resulting in an absorptive resonance with a high quality factor (*Q*-factor; narrow line-width) at near-normal incident angles^{12–16}. As only thin-film deposition is required for fabrication, TPP-EMs can be grown at the wafer scale with relatively low-cost and minimal fabrication steps, offering a promising candidate for WS-EMs^{14–16}.

Despite the broad potential of TPP-EMs, design of such structures is challenging, as most applications require simultaneous control over both emission frequencies and corresponding *Q*-factors, and suppression of emission at other frequencies. Compared with traditional TPP-EMs based on periodic DBRs¹⁷, aperiodic structures provide additional spectral control, allowing for the suppression of spurious emission peaks¹⁸, while simultaneously achieving ultra-high *Q*-factors^{14,15}. However, due to the large parameter space associated with the design of aperiodic DBRs, forward-design methodologies are not efficient and thus, inverse design protocols must

be used, with high-*Q*-factor TPP-EMs demonstrated at a single desired wavelength via Bayesian optimization and a genetic algorithm¹⁸ with high accuracy. However, such earlier works exhibited poor optimization efficiencies, requiring upwards of 24-day-long simulations per optimized structure¹⁴. More importantly, the design of multiple emission peaks, where the frequency, amplitude and line-width of each resonance can be controlled independently, has not been realized. Using such a multi-peak TPP-EM, the sensing of multiple gases of interest simultaneously as well as high-sensitivity gas detection could both be achieved when the TPP-EM resonances were matched to several vibrational modes of one or multiple chemicals. Furthermore, in experimental reports, only noble metals have been used so far, which due to the plasma frequency falling in the visible range thereby severely restricts the spectral control, while also being incompatible with complementary metal-oxide-semiconductor (CMOS) processing.

Here we present an inverse design algorithm to efficiently optimize TPP-EMs composed of an aperiodic DBR grown on an *n*-type, In-doped cadmium oxide (CdO) film, offering individual control of multi-peak WS-EMs. The inverse design protocol is based on stochastic gradient descent (SGD) that allows for the individual layer thicknesses, as well as the carrier density (and thus the dielectric function) of CdO (ref. ¹⁹) to be optimized efficiently (minutes on a consumer-grade desktop). We experimentally validate our design approach and realize single-, dual- and triple-band TPP-EMs over a broad spectral range, with all structures exhibiting excellent agreement between experiments and simulations. Importantly, we numerically verify the advantages of multi-peak TPP-EMs for NDIR applications, such as enabling simultaneous detection of multiple gases with high sensitivity. Furthermore, we illustrate the design

¹Department of Mechanical Engineering, Vanderbilt University, Nashville, TN, USA. ²Interdisciplinary Materials Science Program, Vanderbilt University, Nashville, TN, USA. ³Department of Materials Science and Engineering, Pennsylvania State University, University Park, PA, USA. ⁴Department of Electrical Engineering and Computer Science, Vanderbilt University, Nashville, TN, USA. ⁵Department of Physics and Astronomy, University of Iowa, Iowa City, IA, USA. ⁶These authors contributed equally: Mingze He, J. Ryan Nolen. ✉e-mail: mingze.he@vanderbilt.edu; josh.caldwell@vanderbilt.edu

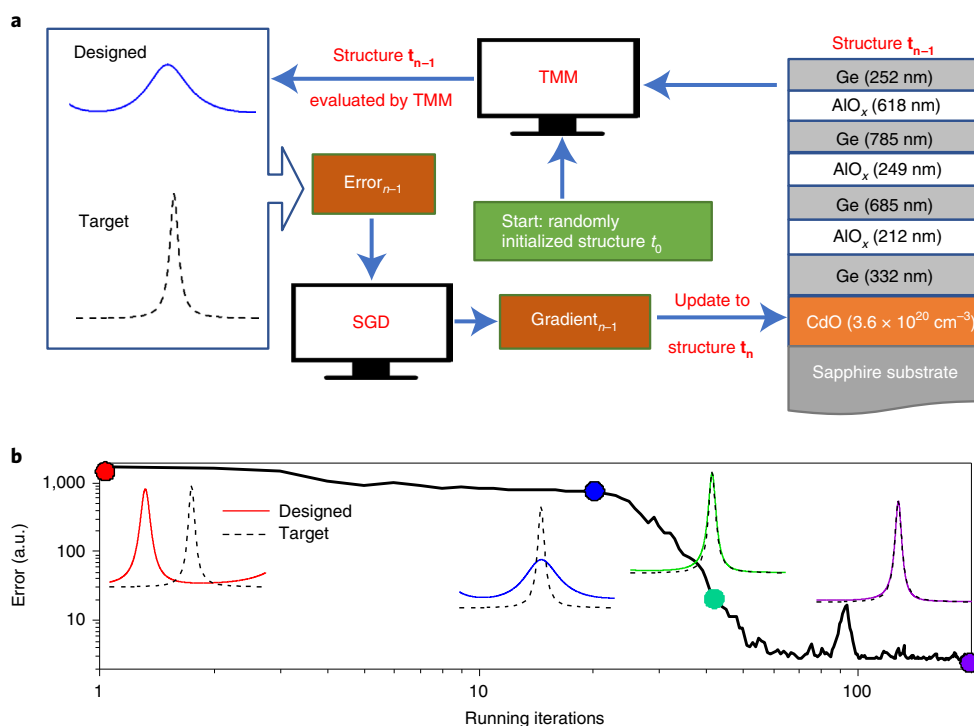


Fig. 1 | Flowchart of the design process. **a**, Left: the designable parameters of the TPP-EM structure (thickness and carrier concentration), \mathbf{t} , are randomly initialized (green box); then it is evaluated by the TMM, resulting in the DS. The DS is compared with the TS, leading to a scalar error. In the current iteration ($n-1$), the gradient of scalar error over \mathbf{t}_{n-1} , that is, $\frac{\partial \text{error}_{n-1}}{\partial \mathbf{t}_{n-1}}$, is calculated by SGD and used to update \mathbf{t}_{n-1} to \mathbf{t}_n by equation (2). The updated \mathbf{t}_n will then be evaluated by TMM, getting a new DS, comparing with TS and updating to a new version; and the process will repeat until a given number of iterations are reached. Right: the optimized structure. **b**, One exemplary optimizing process; the TS are plotted in dashed lines, and the DS are plotted as solid lines with different colours each pertaining to a different point along the iteration path. One photo of the wafer-scale sample is shown in Supplementary Fig. 4.

capabilities of CdO-based TPP-EMs by demonstrating the ability to match the resonant frequencies, line shapes and amplitudes of arbitrarily shaped spectra extending from the LWIR to telecommunication bands, including the ability to define Q-factors over a broad range of values at any given frequency (for example, 27–10,117 was demonstrated at $2,360\text{ cm}^{-1}$). Finally, we stress that such functionality is not possible within noble-metal-based TPP-EMs but instead is enabled by the broadly tunable plasma frequency of CdO (refs. 19–23). The combination of our efficient inverse design algorithm with these material advancements facilitates the realization of cost-effective, wafer-scale, CMOS-compatible and lithography-free TPP-EMs for numerous applications, including multi-gas NDIR; environmental, atmospheric and chemical sensing; free-space communications; and infrared beacons.

SGD-based inverse design protocol

The TPP-EMs discussed here are composed of aperiodic DBRs consisting of Ge and AlO_x alternating layers grown on thin ($\sim 500\text{ nm}$) CdO films on sapphire substrates (Fig. 1a). The individual layer thicknesses and CdO carrier density (thus the dielectric function¹⁹) are all included as design parameters, written as a vector (\mathbf{t}). We employ a SGD-based inverse design technique to determine \mathbf{t} , so that the difference between the absorption spectrum of the designed structure (the designed spectrum, DS) and the target spectrum (TS) is minimized. The design process is initiated by assigning the user-preferred maximum number of layers for the DBR, with \mathbf{t} being randomly initialized. Through the transfer matrix method (TMM), the DS of the corresponding structure \mathbf{t} is calculated and compared to the TS, resulting in a scalar error. The error is written

as a combination of mean-squared error (the first term) and mean absolute error (the second term):

$$\text{Error} = \text{Mean} \left(\text{ratio1} (\mathbf{DS} - \mathbf{TS})^2 + \text{ratio2} |(\mathbf{DS} - \mathbf{TS})| \right) \quad (1)$$

where ratio1 and ratio2 are hyperparameters customized for different purposes, and \mathbf{DS} and \mathbf{TS} are vectors with each element standing for the absorbance at corresponding wavelength. Note this combination of error is commonly employed in the deep-learning field, and related techniques are powerful for optimizing TPP-EM design, such as weighted sampling approaches (Supplementary Section 1). This error is then back-propagated to find the gradient over \mathbf{t} via SGD. Upon each iteration, the gradient is used to update \mathbf{t} :

$$\mathbf{t}_n = \mathbf{t}_{n-1} - \text{step} \frac{\partial \text{error}_{n-1}}{\partial \mathbf{t}_{n-1}} \quad (2)$$

After each successive iteration, the error is decreased, and the iterations will continue until a predefined maximum number. As such, the structure of the TPP-EM will be optimized to a point where the error between the TS and DS is minimized.

While optimization processes take a different form on each run, one example is presented in Fig. 1b. Initially, the absorption spectrum of the randomly initialized structure (red solid line) differs significantly from the TS. After several iterations, the DS converges towards the TS (see solid red \rightarrow blue \rightarrow green \rightarrow purple lines in Fig. 1b). Unlike the canonical gradient descent calculations used in commercial software and previous publications^{24,25}, the SGD approach employed here reduces the possibility of getting trapped at poor

local minimums and improves the optimization performance^{26–29} (Supplementary Section 2). Although our method is still a local optimization, the SGD methodology approaches that of global optimization, offering high accuracy and efficiency compared with other methods (Supplementary Table 1). The code is downloadable from our group website (<https://my.vanderbilt.edu/caldwellgroup/>) as well as *Nature Materials*.

Experimental demonstration of inversely designed TPP-EMs

Based on the inverse design algorithm, several TPP-EM structures were designed and fabricated, exhibiting a wide range of unique spectral features. The CdO carrier densities and the designed and as-grown layer thicknesses of these structures are provided in Supplementary Section 4, and the growth process is discussed in the Methods. Note that more complicated spectra (higher Q -factors, more peaks and so on) can be realized when a DBR featuring more layers is utilized; yet, once a target can be realized with a certain number of layers, adding additional layers does not provide any additional advantage (Supplementary Section 6). Thus, in the experimental demonstrations, we employ the least possible number of layers to match the TS to simplify fabrication. To demonstrate the power of inversely designed TPP-EMs, we first provide an experimental device featuring a single emission peak in the LWIR (800–1,250 cm^{-1}) for free-space communications. We model the TS as a flat line with a single, sharp absorption peak centred at 1,250 cm^{-1} and employ the SGD method to match the DS to the narrowest possible TS line-width (Fig. 2a). Following this optimization, the spectrum of the designed structure exhibits a single peak centred at 1,250 cm^{-1} with a Q -factor of 13, while the experimentally resultant Q -factor is ~ 9 . The target, experimentally measured and calculated spectra based on the designed and as-grown thicknesses all show excellent agreement, with all four exhibiting nearly overlapping resonance lines (Fig. 2a).

In addition to emitters for communications, the LWIR and MWIR contain molecular absorption features; thus, one application of WS-EMs is filterless NDIR gas sensing^{1–3}. A filterless NDIR sensor is composed of a WS-EM, a gas cell and a broadband detector (Supplementary Section 7). The emission frequency of the WS-EM is centred at the absorption frequency of the gas of interest with a sufficiently high Q -factor to eliminate false positives resulting from absorption by other gases present. For such applications, we first demonstrate a heterostructure supporting a single emissivity peak at one absorption band of CO_2 (2,349 cm^{-1}). Again, excellent agreement is observed, with the measured (target) emission peak centred at 2,360 cm^{-1} (2,350 cm^{-1}) with a Q -factor of 21 (40), as shown in Fig. 2b. However, while these single-peak emitters can be efficiently designed with our protocol, they can also be realized via other approaches such as intuition-guided forward design¹⁷, Bayesian optimization^{14,30} and genetic algorithms¹⁸, albeit requiring substantially more effort.

So far, we have demonstrated TPP-EM designs with an isolated, tunable emissivity peak, making these devices suitable for applications such as single, simple gas detection. In addition to the applications enabled by such single-peak TPP-EMs, more advanced functions can be realized via multi-frequency TPP-EMs, such as infrared signature management and multi-channel NDIR. For NDIR, additional emission channels can be used to either detect more gases of interest or enhance the sensitivity to a specific gas by aligning the emission to multiple vibrational modes. Yet, WS-EMs with independent design control for multiple distinct emission peaks have not been previously demonstrated, to our knowledge. We first exemplify the functionality of our TPP-EMs by demonstrating a device suitable for simultaneous SO_2 and CO_2 dual-gas sensing, with the rationale for the TS provided in Supplementary Section 8. Additionally, SO_2 and CO_2 concentrations can be independently evaluated using this TPP-EM operating at different

temperatures (Supplementary Section 9). Here, five dielectric layers were used, yielding a DS with two absorption peaks centred at 1,367 and 2,339 cm^{-1} (Fig. 2c), which closely match the amplitudes, peak positions and full-width-half-maximums (FWHMs) of the TS. The experimental data also agree well, albeit with some minor exceptions. While the centre frequencies are closely matched (1,358 and 2,360 cm^{-1}), some degradation in the Q -factors and emissivity amplitudes are observed. Spectral discrepancies are minimal despite differences between the as-grown and designed thicknesses, indicating robustness against fabrication errors (Supplementary Section 10). Notably, limited thickness error is expected in foundry-level fabrication.

The functionality of the TPP-EM is not limited to dual-band emission, and more bands at user-designed frequencies can be realized. To exemplify this capability, we also modelled a TS featuring three emission peaks centred at the absorption bands of CO and formaldehyde (1,750 cm^{-1} , 2,150 cm^{-1} and 2,800 cm^{-1}), with increasing FWHMs to compensate for the black-body emission shape (20, 30 and 40 cm^{-1} , respectively) imposed on the resultant TPP-EM spectrum. Again, excellent agreement between the TS, DS and experimental structures for the designed TPP-EM is realized for each of the curves (Fig. 2d) with the peak analyses provided in Supplementary Table 3. Although the thickness difference from fabrication shifts one resonance by 70 cm^{-1} , it remains within the formaldehyde absorption band, thereby still allowing enhanced sensitivity for NDIR applications.

The multi-resonance control we demonstrate above is critical for numerous applications such as multi-frequency infrared beacons for encryption purposes and advanced NDIR applications. Here, we theoretically illustrate the implications of our experimental devices in filterless NDIR applications and compare them with conventional NDIR devices enabled by black-body emitters and filters (Supplementary Tables 4 and 5). The advantages of multi-peak TPP-EMs are (1) improved sensitivity when multiple absorption bands are aligned; (2) the potential of multi-gas sensing within a single compact package; and (3) reduced power consumption. Note that the single-peak TPP-EMs provide identical sensitivity with ~ 5 –10 times lower power consumption (Supplementary Fig. 11). Importantly, the angular dispersions of TPP-EMs are inherently low (Supplementary Fig. 12), eliminating issues from viewing angles as well. Thus, the experimentally demonstrated ability to control the emission frequencies with desired Q -factors provides substantial advantages for such applications, including low false-positive rates and high-sensitivity gas sensing of multiple gases simultaneously within a single, compact NDIR package.

Potential for inversely designed TPP-EMs

For advanced WS-EM applications, such as spectral bar-coding and multi-gas sensing, user-defined FWHMs and amplitudes at single or multiple frequencies must be realized. Yet, no earlier design approaches have been proposed to accomplish these tasks with the necessary accuracy, to our knowledge. To address these challenges and demonstrate further the potential of the inversely designed TPP-EMs, we explore the design capabilities by utilizing a Ge/ZnSe DBR with 29 layers on a bilayer of CdO (all designed structures are included in Supplementary Section 14).

First, we demonstrate the outstanding control over the line-width at a fixed frequency, presenting structures with Q -factors ranging from 26 to 10,117 while maintaining near-unity emission for all designs (Fig. 3a and Supplementary Fig. 13). Thus, we show the potential not only to achieve ultra-high Q -factors for Tamm-based structures (fitting in Supplementary Fig. 14), but also to match the required Q -factor at a given frequency. Such a capability is imperative as different applications have varied requirements for signal-to-noise ratio. Building on this, we expand upon the potential for such multi-peak designs, providing a TS that exhibits three

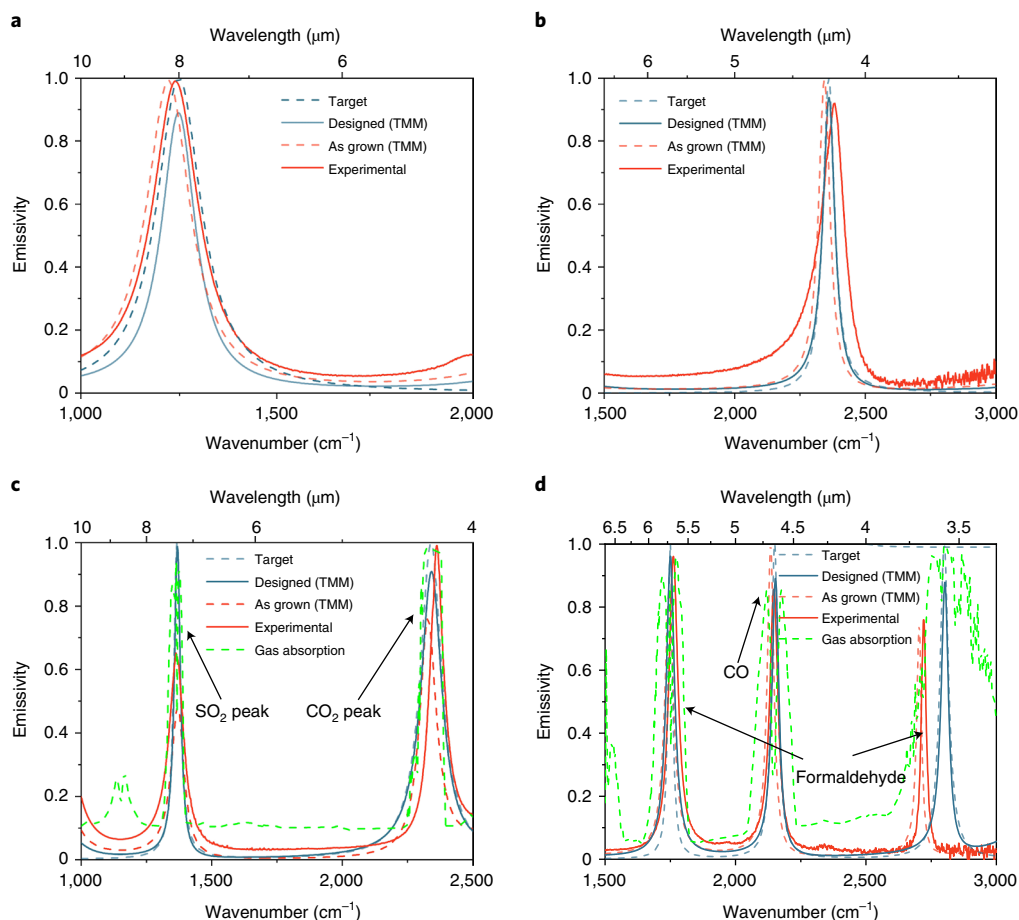


Fig. 2 | Experimental demonstration of TPP-EMs. a–d, The inverse design algorithm was employed to realize TPP-EM structures featuring a single emission mode in the LWIR with a three-layer DBR (**a**) as well as resonant emission designed for NDIR sensing of CO₂ with a three-layer DBR (**b**), CO₂ and SO₂ with a five-layer DBR (**c**) and CO and formaldehyde dual-gas sensing with a seven-layer DBR (**d**). The TS and DS are plotted as blue dashed and solid lines, respectively. The emissivity experimentally measured at 150 °C is plotted as red solid lines, and red dashed lines are the calculated absorption spectra of as-grown structures. Green dashed curves are the combined absorption spectrum of the gases. A photo of the two-inch wafer-scale sample is shown in Supplementary Fig. 4.

emission peaks with varying line-widths (Q -factors = 25, 37 and 145). Such TPP-EM designs are suitable for spectral bar-coding and sensing, yet have not been demonstrated or proposed, to our knowledge, presumably due to the extensive design challenges in matching such complex spectra. Despite this difficulty, the DS can be matched to the TS exceptionally well, with only minor discrepancies (Fig. 3b).

Empowered by the broadly tunable plasma frequency of CdO (between $\sim 1,200$ cm^{-1} and $7,800$ cm^{-1}), TPP-EMs with absorption peaks spanning from the short-wave infrared to the LWIR can also be realized. To demonstrate such capabilities, we optimized another TPP-EM structure featuring three spectrally distinct emission peaks, located in the LWIR ($1,200$ cm^{-1}), MWIR ($2,700$ cm^{-1}) and short-wave infrared (1.55 μm) simultaneously (Fig. 3c). Again, the resultant DS matches the TS exceptionally well. We note that additional modes are present in the spectral regions between these desired emission resonances (Supplementary Fig. 1), which is a fundamental restriction of the multi-modal nature of DBRs. However, the influence of these additional peaks can be mitigated by the weighted sampling technique (Supplementary Sections 1 and 15).

Finally, we emphasize the potential of TPP-EMs in advanced NDIR applications. Here, it is desirable to match the emitted power to the chemical absorption spectra for two reasons: (1) the amount of emitted power should be absorbed as much as possible—that

is, it should emit energy at all chemical absorption bands; and (2) emitted power should only be absorbed by the gas of interest to avoid false positives, meaning the FWHM of the TS cannot be substantially broader than the gas spectra. As the emitted power is temperature dependent, we generalize this concept by matching the TPP-EM to the chemical absorption spectra. One example is provided for nitrogen monoxide NDIR gas sensing in Fig. 3d. This molecule features multiple arbitrarily distributed absorption bands with varying FWHMs and amplitudes between 800 and $2,400$ cm^{-1} , making forward-design approaches unrealistic. Yet, our inverse design algorithm provides an optimized TPP-EM structure with a DS closely matched to the spectral positions, amplitudes and FWHMs of the TS peaks, with undesirable additional modes greatly suppressed (Fig. 3d). The same approach is applied to NDIR sensing of greenhouse gases such as CO, O₃, NH₃ and CH₄, as shown in Supplementary Fig. 16. In addition, the shape of the black-body emission can be deconvoluted in the design process so that the emitted power, rather than the emissivity, can be matched to an arbitrarily shaped TS, which is exemplified for N₂O NDIR sensing at 250 °C working temperature (Supplementary Fig. 17). We would like to stress again that none of the designs in Fig. 3 have been previously proposed, to our knowledge, as the user-defined control of the FWHMs and amplitudes at single/multiple frequencies is not realistic within traditional forward-design approaches. Thus, the design

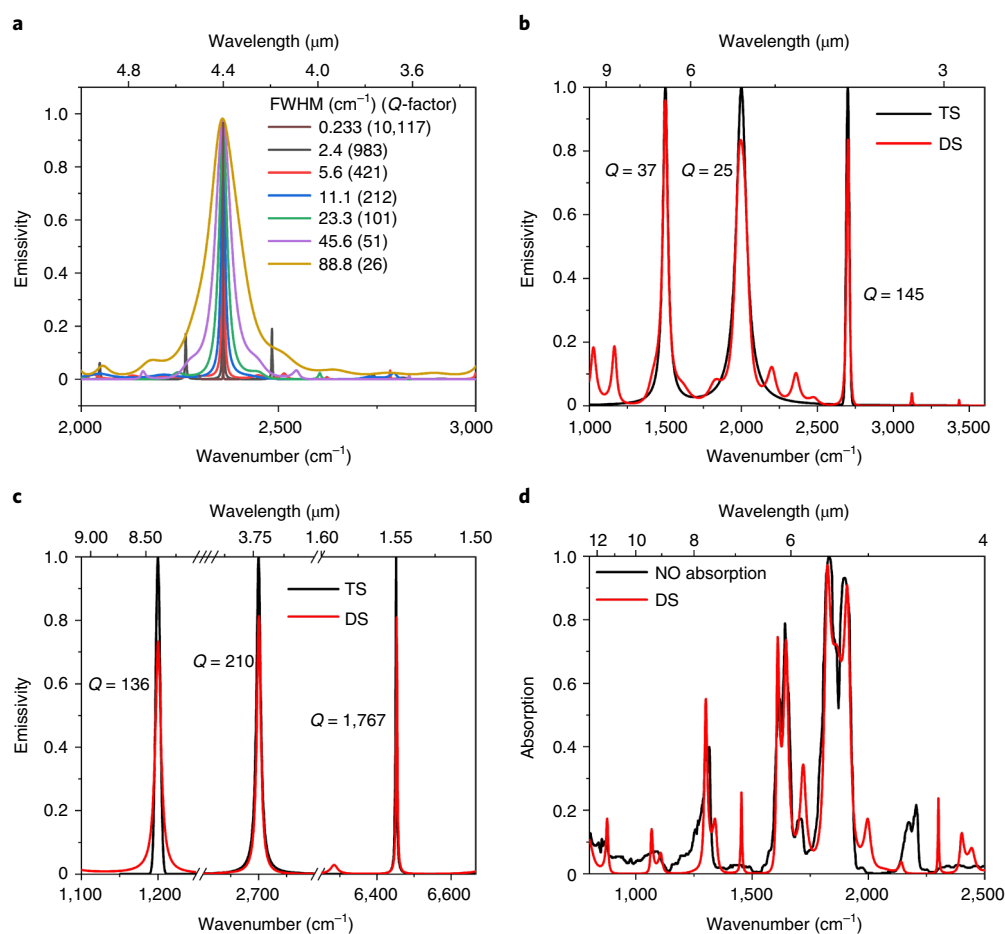


Fig. 3 | Inversely designed TPP-EMs for various applications. **a**, Isolated emission with different Q-factors. The same figure is provided with a narrower frequency range (Supplementary Fig. 13) to show near-unity emission for all of them. **b**, Multiple-peak TPP-EM. **c**, One TPP-EM featuring emissions at LWIR, MWIR and the telecommunication range simultaneously. **d**, Matching the absorption spectrum of nitrogen monoxide (NO) gas for filterless NDIR. The absorption spectrum of NO is normalized to be between 0 and 1.

capabilities highlighted here facilitate WS-EM-based applications for free-space communications, spectral bar-coding, multi-band chemical sensing with high signal-to-noise ratio for highly selective NDIR or alternative gas-sensing metrologies.

CdO as the enabling component for our TPP-EMs

So far, we have demonstrated the exceptional design freedom offered by our inverse design approach for dictating the emissivity and/or spectrally emitted power of TPP-EM devices. The deterministic design capabilities benefit from two things: the SGD-optimized aperiodic DBRs and the use of In-doped CdO with a designable dielectric function. It is the aperiodic DBR that exploits the control over the photonic band structure, yet, it is the designable dielectric function of CdO that improves this spectral control to an unprecedented level, allowing for more advanced designs to be realized. To illustrate this point, we employed our SGD-based algorithm to design a CdO-based and a gold-based TPP-EM to match the absorption spectrum of the nerve agent simulant dimethyl methyl phosphonate for high-sensitivity gas detection. Related detailed optimizations are discussed in Supplementary Section 18. Here, an exceptional agreement between the TS and the CdO-based TPP-EM DS is achieved (Fig. 4a), including spectral positions, line shapes and even amplitudes. However, for the gold-based structure, the absorption spectrum cannot be matched well (Fig. 4a, blue line). This increased spectral control is attributable to the designable plasma frequency of CdO.

To unfold the underlying advantages offered by CdO, we fabricated multiple TPP-EMs composed of the same DBR grown simultaneously on multiple CdO layers featuring different plasma frequencies, that is, $2,700\text{ cm}^{-1}$ (red dashed curve) and $4,300\text{ cm}^{-1}$ (red solid curve; Fig. 4b). Although both samples feature the same DBR structures, the different dielectric functions (carrier concentrations) of CdO result in distinct impedance models for the two systems (Supplementary Section 19). This leads to noticeable differences in the emission spectra, for example, frequencies and amplitudes. Therefore, the adjustable carrier concentrations can tune the TPP and non-TPP modes and thus allow more-arbitrarily-shaped spectra to be matched than what can be achieved with a fixed carrier density. We further performed a series of comparisons among inversely designed TPP-EMs with CdO featuring fixed carrier concentrations and/or mobility (Supplementary Section 20), validating that the tunable dielectric function provides the spectral control necessary for full user design of the emission spectrum amplitudes, line-widths and resonant frequencies. Although the loss of CdO (mobility) affects the TPP-EM^{31–33}, our code and platform can mitigate the influence of this loss by modifying the corresponding carrier density (Supplementary Section 20). As such, the wide tunability of CdO plasma frequency increases the design capability of TPP-EMs to an unprecedented level compared with traditional noble-metal-based TPP-EMs. In addition to the spectral control, replacing the noble metal with n-type In-doped CdO also makes the fabrication process CMOS compatible, potentially permitting

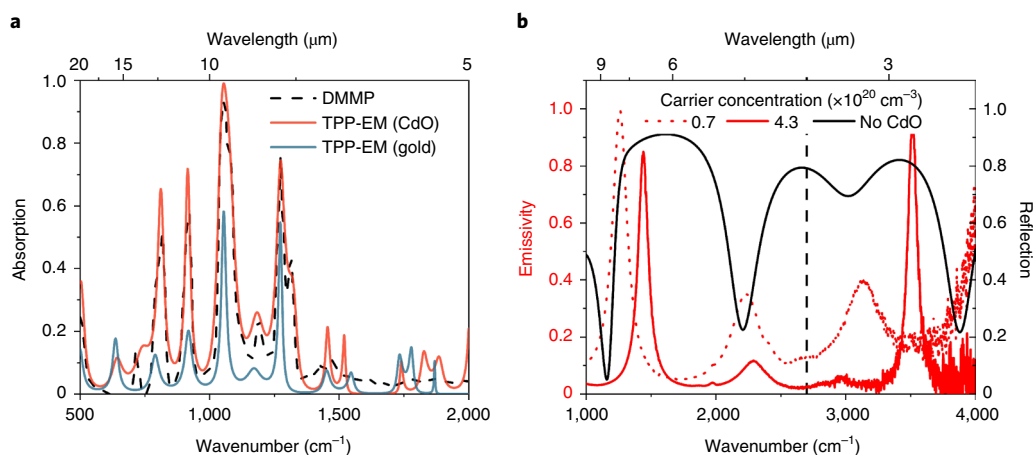


Fig. 4 | Functionality enabled by the tunability of CdO plasma frequency. **a**, TPP-EM designs targeting the dimethyl methyl phosphonate (DMMP) spectrum with CdO and gold as conductive layers. **b**, The emissivity (red lines, experimental data) and reflectance (black lines, calculated by TMM) of the same DBR on CdO layers of different carrier densities and on a sapphire substrate. The plasma frequency of CdO with a carrier density of $7 \times 10^{19} \text{ cm}^{-3}$ is displayed by the vertical dashed line, while the plasma frequency of the other CdO is above $4,000 \text{ cm}^{-1}$. The emissivity of the low-doped CdO has several notable differences from that of the higher-doped heterostructure. (1) The Tamm resonance frequency is lower and exhibits a higher absorption intensity between $1,000$ and $2,000 \text{ cm}^{-1}$; (2) there is a stronger absorption at the reflection dip of the DBR ($\sim 2,300 \text{ cm}^{-1}$), which is not a Tamm mode; and (3) Tamm resonances are not supported above the plasma frequency ($\sim 3,500 \text{ cm}^{-1}$).

integrated applications. Notably, our approach can also be applied to other doped materials, such as III–V semiconductors and other transparent conducting oxides³⁴.

Conclusion

In conclusion, the combination of the broadly tunable plasma frequency of CdO and our efficient SGD-based inverse design enables the deterministic design of TPP-EMs, which is numerically and experimentally validated. Using SGD, the structure of TPP-EMs can be efficiently optimized (minutes on a consumer-grade desktop) for arbitrary TS. Equipped with this method, we experimentally demonstrate single- and multi-band TPP-EMs broadly suitable for different applications, including free-space communications, infrared beacons and single- and multi-gas filterless NDIR sensing, all showing great agreement between experiments and simulations. Importantly, the multi-peak demonstrations open up possibilities for the sensing of multiple gases and single gases with multiple vibrational bands that cannot be achieved with a single-filter, compact NDIR black-body-based device. Further, we illustrate the unprecedented ability of matching the TS, that is, the frequencies, FWHMs and even amplitudes (emissivity or spectral irradiance), by exemplifying several designs ranging from the LWIR to the tele-communications band ($1.55 \mu\text{m}$), including isolated emission at a desired frequency with user-defined Q -factor (from 28 to 10,117), multi-peak emission for spectral bar-codes and NDIR for matching complex gas absorption spectra. Finally, we stress that such broad functionality is not inherent to TPP-EMs; instead, it is enabled by the wide tunability of the CdO plasma frequency. Empowered by our SGD algorithm and this tunability, the demonstrated spectral control of TPP-EMs promises cost-effective, wafer-scale, CMOS-compatible and lithography-free solutions for numerous applications throughout the infrared.

Online content

Any methods, additional references, Nature Research reporting summaries, source data, extended data, supplementary information, acknowledgements, peer review information; details of author contributions and competing interests; and statements of data and code availability are available at <https://doi.org/10.1038/s41563-021-01094-0>.

Received: 18 April 2021; Accepted: 4 August 2021;
Published online: 21 October 2021

References

- Livingood, A. et al. Filterless nondispersive infrared sensing using narrowband infrared emitting metamaterials. *ACS Photon.* **8**, 472–480 (2021).
- Lochbaum, A. et al. On-chip narrowband thermal emitter for mid-IR optical gas sensing. *ACS Photon.* **4**, 1371–1380 (2017).
- Lochbaum, A. et al. Compact mid-infrared gas sensing enabled by an all-metamaterial design. *Nano Lett.* **20**, 4169–4176 (2020).
- Baranov, D. G. et al. Nanophotonic engineering of far-field thermal emitters. *Nat. Mater.* **18**, 920–930 (2019).
- Lu, G. et al. Narrowband polaritonic thermal emitters driven by waste heat. *ACS Omega* **5**, 10900–10908 (2020).
- Howes, A., Nolen, J. R., Caldwell, J. D. & Valentine, J. Near-unity and narrowband thermal emissivity in balanced dielectric metasurfaces. *Adv. Optical Mater.* **8**, 1901470 (2020).
- Kelley, K. P. et al. Multiple epsilon-near-zero resonances in multilayered cadmium oxide: designing metamaterial-like optical properties in monolithic materials. *ACS Photon.* **6**, 1139–1145 (2019).
- Schuller, J. A., Taubner, T. & Brongersma, M. L. Optical antenna thermal emitters. *Nat. Photon.* **3**, 658–661 (2009).
- Wang, T. et al. Phonon-polaritonic bowtie nanoantennas: controlling infrared thermal radiation at the nanoscale. *ACS Photon.* **4**, 1753–1760 (2017).
- Arnold, C. et al. Coherent thermal infrared emission by two-dimensional silicon carbide gratings. *Phys. Rev. B* **86**, 035316 (2012).
- Asano, T. et al. Near-infrared-to-visible highly selective thermal emitters based on an intrinsic semiconductor. *Sci. Adv.* **2**, e1600499 (2016).
- Kaliteevski, M. et al. Tamm plasmon-polaritons: possible electromagnetic states at the interface of a metal and a dielectric Bragg mirror. *Phys. Rev. B* **76**, 165415 (2007).
- Sasin, M. E. et al. Tamm plasmon polaritons: slow and spatially compact light. *Appl. Phys. Lett.* **92**, 251112 (2008).
- Sakurai, A. et al. Ultranarrow-band wavelength-selective thermal emission with aperiodic multilayered metamaterials designed by Bayesian optimization. *ACS Cent. Sci.* **5**, 319–326 (2019).
- Wang, Z. et al. Ultra-narrow and wavelength-tunable thermal emission in a hybrid metal-optical Tamm state structure. *ACS Photon.* **7**, 1569–1576 (2020).
- Wang, Z. et al. Narrowband thermal emission realized through the coupling of cavity and Tamm plasmon resonances. *ACS Photon.* **5**, 2446–2452 (2018).
- Yang, Z.-Y. et al. Narrowband wavelength selective thermal emitters by confined tamm plasmon polaritons. *ACS Photon.* **4**, 2212–2219 (2017).
- Botros, J., Ali, M. O., Tait, R. N., Amaya, R. E. & Gupta, S. Direct thermal emission testing of aperiodic dielectric stack for narrowband thermal emission at mid-IR. *J. Appl. Phys.* **127**, 114502 (2020).

19. Nolen, J. R. et al. Ultraviolet to far-infrared dielectric function of n-doped cadmium oxide thin films. *Phys. Rev. Mater.* **4**, 025202 (2020).
 20. Liu, C. P. et al. Effects of free carriers on the optical properties of doped CdO for full-spectrum photovoltaics. *Phys. Rev. Appl.* **6**, 064018 (2016).
 21. Runnerstrom, E. L., Kelley, K. P., Sachet, E., Shelton, C. T. & Maria, J.-P. Epsilon-near-zero modes and surface plasmon resonance in fluorine-doped cadmium oxide thin films. **4**, 1885–1892 (2017).
 22. Sachet, E. et al. Dysprosium-doped cadmium oxide as a gateway material for mid-infrared plasmonics. *Nat. Mater.* **14**, 414–420 (2015).
 23. Cleri, A. et al. Mid-wave to near-IR optoelectronic properties and epsilon-near-zero behavior in indium-doped cadmium oxide. *Phys. Rev. Mater.* **5**, 035202 (2021).
 24. Xue, W. & Miller, O. D. High-NA optical edge detection via optimized multilayer films. Preprint at <https://arxiv.org/abs/2101.03160> (2021).
 25. Jiang, J. & Fan, J. A. Multiobjective and categorical global optimization of photonic structures based on ResNet generative neural networks. *Nanophotonics* **10**, 361–369 (2021).
 26. Bordes, A., Bottou, L. & Gallinari, P. SGD-QN: careful quasi-Newton stochastic gradient descent. *J. Mach. Learn. Res.* **10**, 1737–1754 (2009).
 27. Sohl-Dickstein, J., Poole, B. & Ganguli, S. Fast large-scale optimization by unifying stochastic gradient and quasi-Newton methods. *Proc. Mach. Learn. Res.* **32**, 604–612 (2014).
 28. Kingma, D. P. & Ba, J. Adam: a method for stochastic optimization. In *3rd International Conference on Learning Representations* (eds Bengio, Y. & LeCun, Y.) ICLR (Poster) (dblep, 2015).
 29. Robbins, H. & Monro, S. A stochastic approximation method. *Ann. Math. Stat.* **22**, 400–407 (1951).
 30. Zhang, W., Wang, B. & Zhao, C. Selective thermophotovoltaic emitter with aperiodic multilayer structures designed by machine learning. *ACS Appl. Energy Mater.* **4**, 2004–2013 (2021).
 31. Brand, S., Kaliteevski, M. A. & Abram, R. A. Optical Tamm states above the bulk plasma frequency at a Bragg stack/metal interface. *Phys. Rev. B* **79**, 085416 (2009).
 32. Morozov, K. M. et al. Revising of the Purcell effect in periodic metal-dielectric structures: the role of absorption. *Sci. Rep.* **9**, 9604 (2019).
 33. Kaliteevski, M. A. et al. Experimental demonstration of reduced light absorption by intracavity metallic layers in Tamm plasmon-based microcavity. *Plasmonics* **10**, 281–284 (2015).
 34. Bikbaev, R. G., Vetrov, S. Y. & Timofeev, I. V. Transparent conductive oxides for the epsilon-near-zero Tamm plasmon polaritons. *J. Opt. Soc. Am. B* **36**, 2817–2823 (2019).
- Publisher's note** Springer Nature remains neutral with regard to jurisdictional claims in published maps and institutional affiliations.
- © The Author(s), under exclusive licence to Springer Nature Limited 2021

Methods

Device fabrication. In-doped CdO (n-type) was deposited on two-inch *r*-plane (012) sapphire single-crystal substrates at 400 °C by a reactive cosputtering process employing high-power impulse magnetron sputtering and radio frequency sputtering from two-inch-diameter metal cadmium and indium targets, respectively. High-power impulse magnetron sputtering drive conditions were 800 Hz frequency and 80 μs pulse time, yielding a 1,250 μs period and 6.4% duty cycle. Film growth occurs in a mixed argon (20 sccm) and oxygen (14.4 sccm) environment at a total pressure of 10 mtorr. Post deposition, samples were annealed in a static oxygen atmosphere at 635 °C for 30 min.

Dielectric stacks (Ge and AlO_x) were deposited at ambient temperature using electron beam evaporation from Ge (99.999%) and sapphire sources in vacuum. Thickness was monitored throughout the deposition using a quartz crystal microbalance. Post deposition, samples were cleaved and the layer thicknesses were measured using cross-sectional scanning electron microscopy.

Thermal emission measurements. All the thermal emissions were measured at normal incident angle. Thermal emission was measured using a Bruker VERTEX 70v Fourier transform infrared (FTIR) spectrometer by placing our device on a vertically oriented temperature controller located at the back port of the FTIR. The emission from the sample was then guided and collected through a KBr window and into the FTIR internal beam path. In this configuration the emitted signal passes through the interferometer block, taking the place of the spectrometer's internal broadband source, which is turned off. An aperture was placed in the sample compartment to limit the detected solid angle from the device and reduce the detected emission from within the FTIR. The signal was measured using an IR Labs mercury–cadmium–telluride detector. In order to calculate the emissivity, thermal emission measurements were collected from our device at 150 °C. These measurements were then compared to the thermal emission measured from an emissivity standard at the same temperature and angle of emission. We used 500-μm-tall vertically aligned carbon nanotubes grown on a Si substrate from an Fe-nanoparticle catalyst, grown by Nanotechlabs, as an emissivity standard ($\epsilon \approx 0.97$). These vertically aligned carbon nanotubes (VACNT) provide a high, consistent value for emissivity that is spectrally flat throughout the infrared and stable with temperature. The signal collected by the mercury–cadmium–telluride detector in these measurements contains the emission from both the sample as well as the internal optics of the FTIR.

$$M(T_{\text{sample}}, T_{\text{ambient}}, \lambda, \theta) = R(T_{\text{ambient}}, \lambda) (S(T_{\text{sample}}, \lambda, \theta) + G(T_{\text{ambient}}, \lambda)) \quad (3)$$

Here M is the total measured signal, R is a response function for the internal and external optics, S is the signal originating from the sample and G is the 'background' emission from the internal optics. θ is the measured emission angle, λ is the corresponding wavelength, T_{ambient} is the ambient temperature and T_{sample} is the sample temperature. Thus, to isolate the signal from the sample, a background measurement was taken by replacing the sample with a gold mirror. The resultant spectrum is a product of the response function R with the background emission G . Once the sample, emissivity standard and background emission have been measured, we can rearrange equation (3).

$$R(T_{\text{ambient}}, \lambda) S_{\text{sample}}(T_{\text{sample}}, \lambda, \theta) = M_{\text{sample}}(T_{\text{sample}}, T_{\text{ambient}}, \lambda, \theta) - R(T_{\text{ambient}}, \lambda) G(T_{\text{ambient}}, \lambda) \quad (4)$$

$$R(T_{\text{ambient}}, \lambda) S_{\text{standard}}(T_{\text{sample}}, \lambda, \theta) = M_{\text{standard}}(T_{\text{sample}}, T_{\text{ambient}}, \lambda, \theta) - R(T_{\text{ambient}}, \lambda) G(T_{\text{ambient}}, \lambda) \quad (5)$$

where M_{standard} and S_{standard} are the total measured signal and the signal originating from the standard blackbody (VACNT), respectively. The response function can be normalized out by taking the ratio of equations (4) and (5), and the emissivity relative to the standard can be determined.

$$\frac{R(T_{\text{ambient}}, \lambda) S_{\text{sample}}(T_{\text{sample}}, \lambda, \theta)}{R(T_{\text{ambient}}, \lambda) S_{\text{standard}}(T_{\text{sample}}, \lambda, \theta)} = \frac{S_{\text{sample}}(T_{\text{sample}}, \lambda, \theta)}{S_{\text{standard}}(T_{\text{sample}}, \lambda, \theta)} = \epsilon(T_{\text{sample}}, \lambda, \theta) \quad (6)$$

Note that this technique is much quicker than the conventional approach to measuring emissivity using FTIR and allows for multiple background measurements to be taken throughout the day. Therefore, fluctuations in the ambient temperature can be accounted for readily.

Numerical calculation of TPP-EMs. The TMM calculation employed in the inverse design is from textbooks. As the materials are absorbing and dispersive, TMM calculations performed in this paper are from refs. 35,36 for cross-validation purposes, and codes are offered by N. Passler and A. Paarmann. The dielectric functions of Ge and AlO_x are fitted with ellipsometry measurements with WVase software from J.A. Woollam³⁷, and temperature-dependent values are adjusted with reflectance data (Supplementary Section 5). The dielectric function model

of CdO with varying carrier concentration is from ref. 19 from our group, and a corresponding MATLAB code to generate CdO dielectric functions in the MWIR–LWIR is provided on our group website (<https://my.vanderbilt.edu/caldwellgroup/>). The Outlook section treats the dielectric function of Ge (ref. 38) and ZnSe (ref. 39) as constants in the entire frequency range: 16 + 0i and 5.0625 + 0i, respectively.

Computation resources used for the algorithm. All the optimizations are performed on a consumer-grade desktop equipped with an Intel I7-8700K CPU (~US\$400 when first launched in 2017) and 16 GB memory, and no GPU units are used. The algorithm is written in Python 3.6 with TensorFlow 2.3.0. The specific SGD version we use is adaptive momentum estimation (Adam), provided by TensorFlow, and the optimization step is 0.005. All optimizations performed in this paper took ~1–10 minutes. We would like to stress again that the code is open-sourced on our group website (<https://my.vanderbilt.edu/caldwellgroup/>) and the *Nature Materials* website and can be freely used for non-profit purposes.

Absorption data of various chemicals. All chemical absorption spectra are taken from the National Institute of Standards and Technology website.

Data availability

The authors declare that the data supporting the findings of this study are available within the paper and its supplementary information files. Additional data is available from the authors upon request.

Code availability

The algorithms used for this work are available within the paper as well as at our group website (<https://my.vanderbilt.edu/caldwellgroup/>).

References

- Passler, N. C. & Paarmann, A. Generalized 4×4 matrix formalism for light propagation in anisotropic stratified media: study of surface phonon polaritons in polar dielectric heterostructures. *J. Opt. Soc. Am. B* **34**, 2128–2139 (2017).
- Passler, N. C., Jeannin, M. & Paarmann, A. Layer-resolved absorption of light in arbitrarily anisotropic heterostructures. *Phys. Rev. B* **101**, 165425 (2020).
- Li, H. H. Refractive index of silicon and germanium and its wavelength and temperature derivatives. *J. Phys. Chem. Ref. Data* **9**, 561–658 (1980).
- Burnett, J. H., Kaplan, S. G., Stover, E. & Phenis, A. Refractive index measurements of Ge. *Proc. SPIE* **9974**, 99740X (2016).
- Gao, W. Spectroscopic ellipsometry studies on vacuum-evaporated zinc selenide thin film. *Proc. SPIE* **7283**, 72832L (2009).

Acknowledgements

M.H., J.R.N., J.-P.M., A.C. and J.D.C. gratefully acknowledge support for this work by Office of Naval Research grant N00014-18-1-2107. J.-P.M. and J.N. acknowledge support from the Army Research Office research grant W911NF-16-1-0406. J.N. gratefully acknowledges support from the Department of Defense through the National Defense Science and Engineering Graduate Fellowship Program. Y.T. and B.A.L. thank the National Science Foundation for support (NSF 1452485). Funding for G.L. was provided through a Small Business Technology Transfer programme provided by the National Science Foundation, Division of Industrial Innovation and Partnerships (award no. 2014798). T.G.F. was supported by Vanderbilt University through J.D.C.'s start-up package. We thank the National Institute of Standards and Technology for providing the infrared absorption spectra of chemicals and N. Passler and A. Paarmann of the Fritz Haber Institute for their TMM code^{35,36} to validate our work.

Author contributions

M.H., J.R.N., J.D.C. and J.-P.M. conceived the idea. M.H. developed the algorithm. J.R.N. and M.H. performed the infrared measurements. M.H. analysed the dependence of TPP-EM on CdO properties, and J.R.N. performed the analysis from a physics perspective. J.N. and A.C. fabricated the samples, and N.S.M. characterized the sample topography. M.H. and Y.T. completed the theoretical analysis regarding the algorithm. M.H. and G.L. performed the NDIR evaluation. All participated in the writing.

Competing interests

The authors declare no competing interests.

Additional information

Supplementary information The online version contains supplementary material available at <https://doi.org/10.1038/s41563-021-01094-0>.

Correspondence and requests for materials should be addressed to Mingze He or Joshua D. Caldwell.

Peer review information *Nature Materials* thanks Juerg Leuthold, Changying Zhao and the other, anonymous, reviewer(s) for their contribution to the peer review of this work.

Reprints and permissions information is available at www.nature.com/reprints.